Experimentation and simulation of a swirled burner featuring cross-flow hydrogen injection with a focus on the OH* chemiluminescence

Boris Kruljevic, Nasser Darabiha, Daniel Durox, Nicolas Vaysse, Antoine Renaud, Ronan Vicquelin, Benoît Fiorina

Graphical Abstract

Experimentation and simulation of
a swirled burner featuring cross-flow hydrogen injection
with a focus on the OH* chemiluminescence

Boris Kruljevic, Nasser Darabiha, Daniel Durox, Nicolas Vaysse, Antoine Renaud, Ronan Vicquelin, Benoît Fiorina

Highlights

Experimentation and simulation of
a swirled burner featuring cross-flow hydrogen injection
with a focus on the OH* chemiluminescence

Boris Kruljevic, Nasser Darabiha, Daniel Durox, Nicolas Vaysse, Antoine Renaud, Ronan Vicquelin, Benoît Fiorina

- A partially-premixed hydrogen-air flame featuring cross-flow hydrogen injection is characterized numerically, for the first time.
- Analysis of the mixing mechanism inside and at the outlet of the burner.
- Numerical comparison between the HRR distribution and the OH* emission.
- Determination of the relationship between the HRR and the OH* emission in a 1-D strained counterflow flame.

Experimentation and simulation of a swirled burner featuring cross-flow hydrogen injection with a focus on the OH* chemiluminescence

Boris Kruljevic, Nasser Darabiha, Daniel Durox, Nicolas Vaysse, Antoine Renaud, Ronan Vicquelin, Benoît Fiorina

[a]*Laboratoire EM2C, CNRS, CentraleSupélec, Université Paris-Saclay, Gif-sur-Yvette, 91190, France*

Abstract

Large eddy simulations (LES) and experimental measurements were conducted on a swirled partially-premixed hydrogen-air flame with cross-flow hydrogen injection at two different lean operating points, to have two types of flames. This study represents the first simulation of this configuration using hydrogen as the sole fuel. Flame chemiluminescence is used to observe the OH* emission and the light of burnt gases in the visible range. Velocity profile measurements are conducted to validate the results of Large Eddy Simulation (LES). In cold conditions, the burner is analyzed for the two operating conditions in terms of local equivalence ratio distribution and flow field. The analysis demonstrates that the mixing at the burner outlet is relatively efficient, despite the late cross-flow injection of hydrogen and the low inertia of this gas. This efficiency is attributed to the recirculating zone induced by the swirl flow and to the small convergent nozzle at the burner outlet. The reactive flow is then studied at the two operating conditions by analysing velocity, local equivalence ratio, OH* emission and heat release rate (HRR) distribution. Numerical simulations are in good agreement with

the experiments. Compared to images of visible burnt gases, the simulations have successfully reproduced the flame shapes observed experimentally. Although the two operating conditions appear to be stabilized in a different manner from the OH* images, one giving a lifted flame and the other is attached, the LES revealed that both flames are attached to the injector tip. This was observed from the presence of significant heat release rate inside of the injector for both operating conditions. The differences between the OH* emission and the heat release rate localization obtained by the LES are then discussed. 1-D calculations carried out in a strained counterflow flame configuration are used to interpret them. 1-D calculations indicate that the maximum OH* level is not at the same equivalence ratio as the maximum HRR level, and that the OH* level decreases much faster than that of HRR on the rich flame side. 1-D calculations also show that a non-negligible OH* emission also exists in the burnt gases of hydrogen-air flames close to stoichiometry. For highly preheated mixtures, the OH* concentration in burnt gas can be even higher than in the flame front.
Keywords: Partially premixed H2-air flames; swirl burner; cross-flow injection, OH* emission.

Novelty and Significance Statement

The study presents two novelties. Firstly, it shows the simulation of a swirled hydrogen burner, which involves injecting hydrogen radially into air before ignition, both in cold and reacting conditions. The second major innovation involves the connection between the heat release rate (HRR) and OH*, in partially premixed hydrogen-air flames. The OH* was found to be an ineffective tracer for HRR in rich regions. On the other hand, in lean re-

gions the evolutions of OH* and HRR as a function of the equivalence ratio are somewhat similar. This was then analyzed through 1-D computations for various strain rates. Furthermore, simulations indicated the presence of a substantial amount of OH* in the burnt gases when conditions are close to stoichiometry. Experimental validation of this simulation result was performed using a fully-premixed hydrogen flame.

Author Contributions

- BK performed the LES, performed 1-D simulations, analyzed the results, wrote the paper
- ND performed 1-D simulations, analyzed the results, edited the paper
- DD designed the burner, performed experiments, edited the paper
- NV performed experiments, processed data, analyzed data, edited the paper
- AR supervised the research, obtained funding
- RV supervised the research
- BF analyzed the data, supervised the research, obtained funding

1. Introduction

The interest in hydrogen combustion is rapidly growing in the combustion community due to ongoing decarbonization efforts. Numerous issues must be addressed to design safe and practical combustors, the fuel injection

technique and the stabilization of hydrogen-air flames being not trivial. Additionally, the high flame temperature of hydrogen-air mixtures can lead to significant NOx emissions through the thermal oxidation mechanism. The temperature is closely related to the equivalence ratio, so the way hydrogen is mixed with the oxidizer before ignition is crucial. Therefore, it is preferred to promote lean conditions where the temperature is low and the laminar flame velocity is reduced. In addition, burners must be designed to avoid flashback as well as thermo-acoustic instabilities.

Among the possible injection strategies, one approach is to mix the reactants well upstream of the burner to avoid the high-temperature zones of nonpremixed flames. This first strategy requires perfect control of flashback and relies on a detailed characterization of the burner operating regimes. This has been done, for example, by Sattelmayer et al. [1] with a swirl burner, by Day et al. [2] with a low swirl burner or by Yang et al. [3] with a swirl burner equipped with a bluff-body. However, this strategy is risky, and it is generally not advisable to have a sizable amount of hydrogen/air mixture inside the system. Flashback is always a threat, despite the progress made on the fundamental understanding of this mechanism [4, 5].

To avoid complete premixing in the pipes, the second technique involves mixing the reactants slightly before they reach the burner outlet. The challenge lies in efficiently mixing the reactants over a short distance and in a small volume. To achieve this, swirling flows can be used. For example, in [6, 7, 8], burners with co-axial swirled injection are studied, with one swirler on the axial hydrogen stream and a second swirler on the annular air stream. This type of injection helps to create the mixture at the burner outlet, but it

does not lead to a complete premixing as can be inferred from spatial maps representing the Takeno index provided in [6]. With this type of burner, the mixing is not complete, but it may be improved with a recess of the hydrogen injection unit relative to the burner outlet [6]. The second injection strategy also includes the Micromix type configuration [9, 10]. This technology uses numerous small exit holes to improve mixing by ensuring contact between air and hydrogen in various areas while also maintaining safety in relation to flashback. The aim of the short residence time of reactants in the combustion zone is to minimize the formation of NOx. This approach, initially designed for hydrocarbon injection, has also been utilized with direct hydrogen injection [11]. However, incomplete mixing persists, primarily due to the low inertia of pure hydrogen.

The approach used in the present study involves injecting hydrogen late in cross-flow, in highly swirled air, and then enhancing the mixing process by narrowing the burner outlet section. Previous experimental observations on this so-called SICCA-H2 burner, have shown that this burner design leads to relatively low NOx levels [12] and a correct flame stabilization [13, 14]. A similar cross-flow injection in a swirling stream was also investigated in [15], but with a mixture of methane and hydrogen, diluted with CO_2 and N_2 but not with pure hydrogen. It is essential to precisely characterize the mixture's quality and examine the flow dynamics and temperature inside and at the burner outlet.

In such burners, the stabilization mechanism is strongly sensitive to the mixing efficiency. The design of the injection system requires the identification of the areas where chemical conversion occurs and heat is released.

However, obtaining experimental information on HRR is challenging. In the case of hydrocarbon/air flames, laser-induced fluorescence (LIF) of OH combined with LIF of CH_2O can provide relatively precise information on the HRR location [16, 17]. But this technique requires the presence of carbon atoms in the fuel, making it inapplicable to hydrogen flames. Experimentalists have long sought to use flame chemiluminescence to directly deduce information on the distribution of HRR [18, 19, 20, 21, 22], but also some indications on the equivalence ratio, and even on the strain rate [23, 24]. For fully premixed hydrocarbon flames subjected to low levels of stretch, it is considered that markers like OH* or CH* evolve as the heat release rate [18], even though it has been observed in [20, 25] that there is an impact of turbulence on the correlation between OH* and HRR in a lean turbulent methane-air flame. When the mixture is stratified or the combustion is diluted, the direct connection between OH* and HRR is lost [26].

The literature on the OH* and HRR correlations for hydrogen flames is however much more limited than for hydrocarbon flames. We can nevertheless note the study [6] which shows a relative similarity between the calculated HRR zone and the OH* emission zone, observed experimentally, in the case of a hydrogen-air flame with a late premixing carried out by swirled coaxial injections. However, in a recent article [27], published by the same group on a laminar premixed hydrogen-air flame, it is shown that the two peaks, that of OH* and that of HRR, are not exactly at the same location in the flame front. The authors observe that the HRR peak is located upstream the OH* peak of about 2 tenths of mm for lean, rich and stoichiometric H2-air flames. This observation leads them to conclude that OH* is therefore not a good

marker of HRR for premixed flames. Given the need to know where the HRR takes place and knowing that it is easy to visualize the OH* emission, it is important to examine this issue in more depth and establish the link between these two quantities in the case of a partially premixed hydrogen-air flames.

This article aims to further investigate the turbulence flame structure of the SICCA-H2 burner with the help of well-resolved Large Eddy Simulations. Two operating conditions will be computed and analyzed in regard with experimental observations in order to understand the fuel-air mixing process and its impact on the flame heat release. A focus will be made on the relation between the location of OH* and HRR.

The paper is organized as follows. First, the experimental setup is described in Sec. 2. Computational details, such as numerics and the modelling methods, are given in Sec. 3. The LES results are presented and compared with experimental results in Sec. 4. In Sec. 5, an analysis is carried out using a 1-D model of species production to highlight the link that exists between OH* and HRR. Part of this section is devoted to showing the existence of OH* emission in the burnt gases of H2/air flames close to stoichiometry.

2. Experimental Setup

The SICCA-H2 burner, shown in Fig. 1, uses a cross-flow injection of hydrogen into a swirling air flow. The tangential swirler, referred to as 707 in [28], has a swirl number of $S = 0.6$ and a pressure loss coefficient $\sigma = \Delta p/[(1/2)\rho U_b^2] = 3.25$. The hydrogen is injected radially from the central tube through six radial holes with a diameter $d_i = 1.5$ mm, as depicted in Fig. 1. The SICCA burner has previously been utilized for spray and

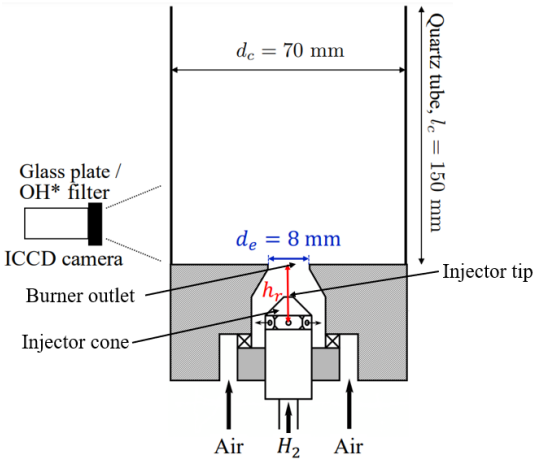

Figure 1: Schematics of the SICCA-H2 burner.

premixed hydrocarbon flames [28]. A significant benefit of this burner is that the tangential swirler can be readily swapped with another to adjust the swirl intensity. Additionally, the injector recess, which is the distance h_r between the center of the hydrogen injection orifices and the burner outlet, can be modified using a screw system. For the current experiment, h_r is fixed at 11.1 mm.

The OH* chemiluminescence signal is captured using a Princeton Instruments PI-MAX4-SB intensified camera fitted with an Asahi Spectra XBPA 310 optical bandpass filter. This filter can be substituted with a glass plate to block UV emission while allowing the visible emission of the flame to pass through, as the camera sensor is only sensitive to light up to 700 nm.

The velocity profiles are obtained in cold conditions using Laser Doppler Anemometry (LDA), by seeding the air flow with micron-sized oil droplets.

This configuration has been studied for a variety of equivalence ratios and thermal powers. More information on flame stability and shape can be found

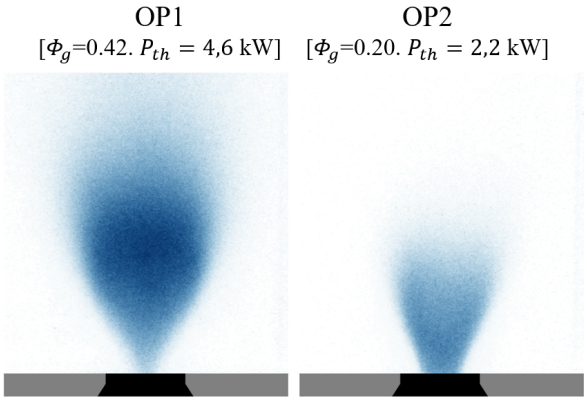

Figure 2: Appearance of the two flames in the visible domain. The images are acquired with an intensified camera. The flames are presented in false colors. On the left, operating point OP1; on the right, operating point OP2. The light corresponds to the continuum blue emission of lean hydrogen-air flames, mainly due to the hydrogen peroxide emission [29, 30].

in [13]. Amongst these conditions, two stable operating points are chosen to be studied in the present work. They are summarized in Table 1. The two flames are shown in Fig. 2. OP1 produces a flame that appears detached from the burner in the visible emission. OP2 results in a V-shaped flame, attached to the burner, with part of the flame inside it.

3. Computational details

The computations are performed with the YALES2 code [31], using the variable-density solver (VDS), which solves low Mach Navier-Stokes equations with a variable density. The temporal evolution is performed using a fourth order scheme, while the spatial terms are discretized with a fourth order central scheme. The subgrid-scale Reynolds Stresses are closed by the Dynamic Smagorinsky model [32].

Table 1: Details for the two operating points under study.

Name	OP1	OP2
Global equivalence ratio	0.42	0.20
Thermal power (kW)	4.6	2.2
Volumetric flow rate of air (NL/min)	146	146
Volumetric flow rate of H2 (NL/min)	26	12.4

The latest version of the UCSD chemical reaction scheme [33], including 10 species and 23 elementary reactions, is used to represent hydrogen-air combustion. This mechanism has been used extensively in hydrogen-air flames [34, 35, 36]. The OH* sub-mechanism given in [37] including 9 reactions (Table 2) is added to the UCSD scheme. The OH* sub-mechanism was applied in [27] for a partially-premixed hydrogen-air flame. The reaction R2, as indicated in references [38, 19], is considered to be irreversible.

Table 2: The OH* sub-mechanism from [37] used in the current study. Details on the reaction rate coefficient k = AT^n exp(–E/RT) are presented.

	Reaction	A (cm mol s)	n	E (kJ mol^-1)
R1	H + O + M(1) $\rightleftharpoons M(1) + OH*$	1.50E+13	0.0	25.0
R2	OH* $\rightarrow OH + hv$	1.45E+06	0.0	0.0
R3	OH* + O_2 $\rightleftharpoons OH + O_2$	2.10E+12	0.0	0.0
R4	OH* + H_2O $\rightleftharpoons OH + H_2O$	5.93E+12	0.5	–2.0
R5	OH* + H_2 $\rightleftharpoons OH + H$	2.95E+12	0.5	–1.9
R6	OH* + N_2 $\rightleftharpoons OH + N$	1.08E+11	0.5	–5.2
R7	OH* + OH $\rightleftharpoons OH + OH$	6.01E+12	0.5	–3.2
R8	OH* + H $\rightleftharpoons OH + H$	1.31E+12	0.5	–0.7
R9	OH* + Ar $\rightleftharpoons OH + Ar$	1.69E+12	0.0	17.3

The Charlette subgrid-scale flame wrinkling model [39] accounts for turbulence-chemistry interactions. We ensure flame resolution by using the dynamic Thickened Flame model for LES [40], which locally adapts artificial thickening based on the grid size and the laminar flame thickness estimated from 1-D freely propagating laminar flamelets.

Surface thermocouple measurements show that the temperatures on the bottom plate of the combustion chamber were approximately uniform and equal to 840 K for OP1 and 550 K for OP2 respectively. These values have been prescribed to all combustion chamber walls as Dirichlet, except for the injector tip which is essentially adiabatic.

In both OP1 and OP2 simulations, the cell size in the flame region is 0.1 mm, which is smaller than the flame front thickness (about a few tenths of a mm). 20 cells are used for the holes where hydrogen is injected into the air for both operating points. The computational grid is larger in OP1 (about 26 million cells) than in OP2 (about 22.5 million cells) because the V-shaped flame is a bit shorter than the lifted one. The maximum thickening factor is kept below 8 for OP1 and below 5 for OP2.

4. Results

4.1. Characteristics of the flow field in cold conditions

To validate the LES results, velocity profiles measured at 2.5 mm downstream of the burner, and under non reacting conditions, have been compared with the numerical velocity profiles. For these experiments, only air (no hydrogen) was sent with a flow rate corresponding to that of operating points OP1 and OP2 (146 NL/min, as shown in Table 1).

The strong agreement between the LES and experiments indicates that the flow field is accurately computed by the simulations for both the mean velocity profiles and the profile of the root mean square (RMS) values of the axial velocity. The agreement is not as good near the axis for the RMS values of the tangential component. These values are a little high compared to the values calculated by LES. However, this discrepancy may be due to insufficient convergence of the measurements in this area. The tangential velocities are low near the axis, and the counting rate of the seeding droplets for the laser velocimetry system is not very high at this location. Apart from this small disagreement, we can consider that the LES simulation predicts the hydrodynamic field of this flow accurately.

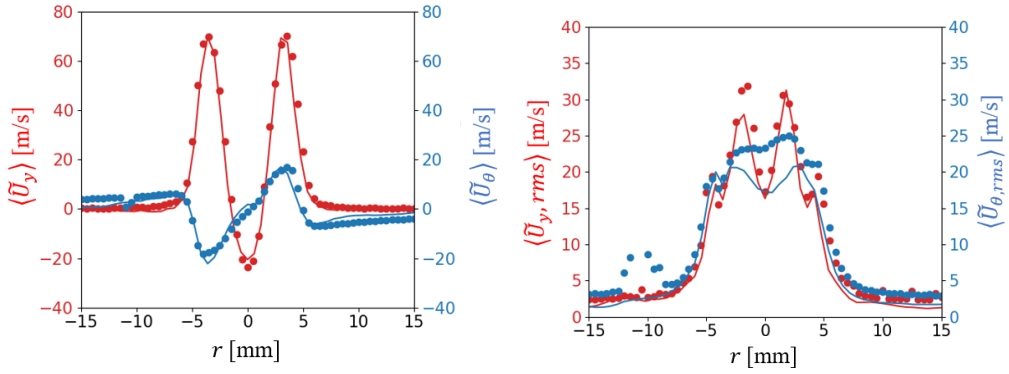

Figure 3: Comparisons between the axial and azimuthal mean (left) and fluctuating (right) velocities obtained in cold conditions from LES (solid lines) and experiments (markers), at 2.5 mm downstream of the burner outlet. The air flow rate corresponds to that of operating points OP1 and OP2. There is no H2 injection.

To understand the mixing mechanisms, Fig. 4 shows the axial velocity fields and velocity streamlines for operating conditions OP1 and OP2. Looking at the injection of hydrogen into the swirling air flow, we can see that in

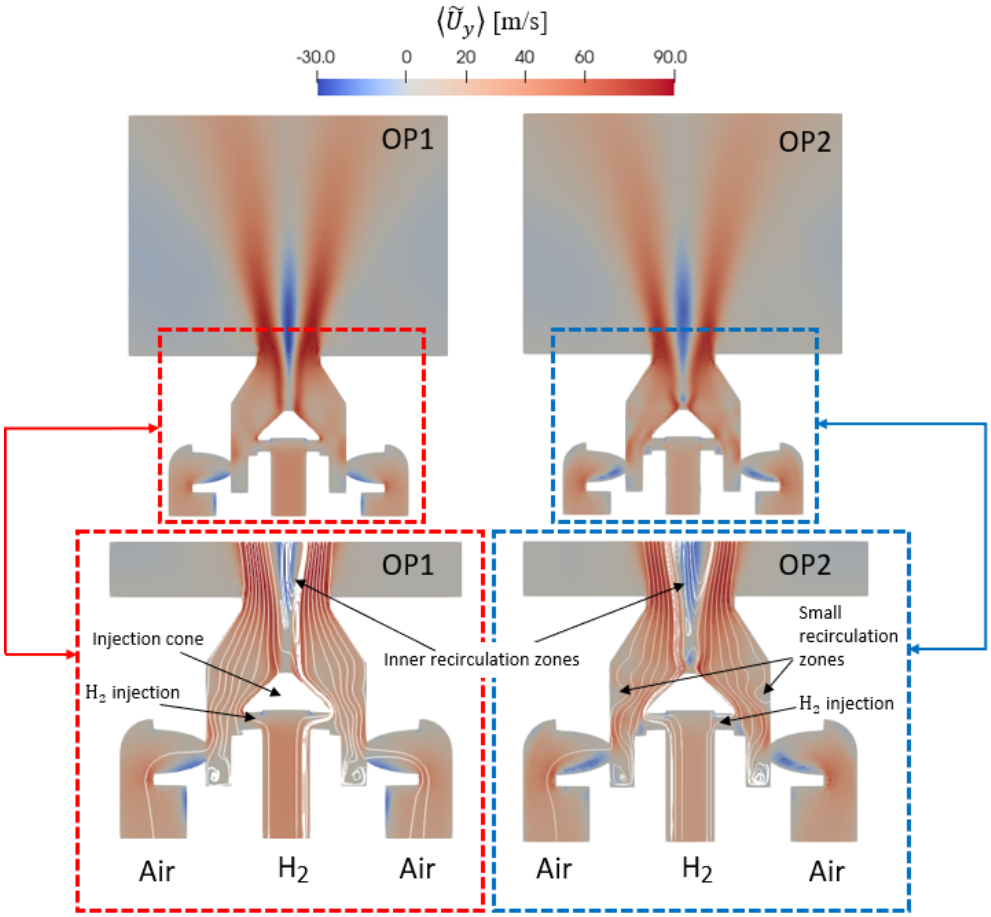

Figure 4: LES axial velocity fields in cold conditions, plotted simultaneously with velocity streamlines in the burner for OP1 (left) and OP2 (right).

the case of OP1, despite the hydrogen flow comes out the injector cone at a velocity of about 55 m/s, it is unable to penetrate the air flow. Air occupies a large space in the cavity around the hydrogen injection cone (in white in the figure)). For OP2, the hydrogen penetration length is even lower (27.5 m/s), which allows the air streamlines to come very close to the white cone. The air passage is less constrained in the OP2 case than in the OP1 case and

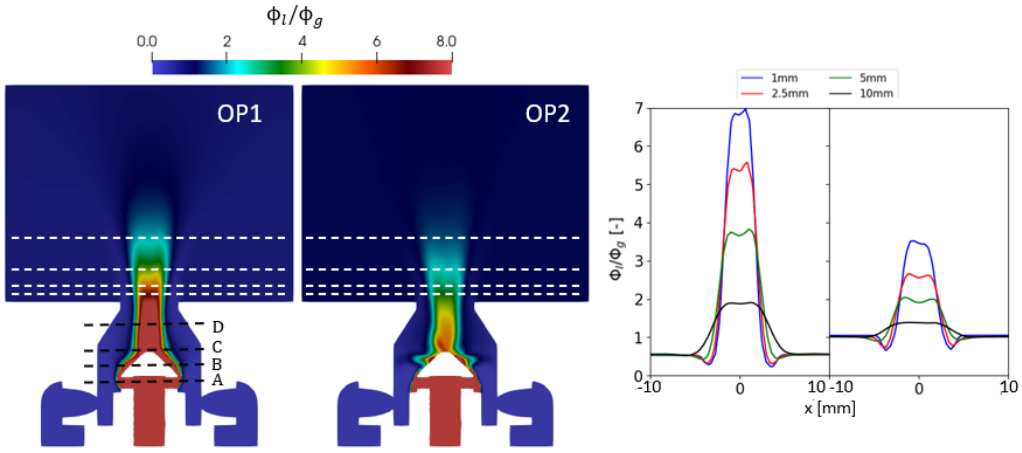

Figure 5: Mean relative equivalence ratio fields for OP1 (left) and OP2 (center) in cold conditions. Φ_l is the mean local equivalence ratio. Φ_g is the global equivalence ratio, i.e. 0.42 for OP1 and 0.2 for OP2. The dashed lines represent the distances from the injector outlet at which the radial profiles of ϕ_l/ϕ_g are plotted in the right figure. They are located at 1 mm, 2.5 mm, 5 mm and 10 mm above the burner outlet. The burner outlet diameter is 8 mm.

we see, for the OP2 case, air flow separations appear in the angle located at the entrance of the convergent nozzle, creating a small recirculating zone (see bottom right in Fig. 4). The lack of similar recirculating zone for OP1 is due to the higher flow rate of hydrogen in the burner cavity and therefore a slightly narrower passage for the air. This was verified by performing simulations (not presented here) without any injection through the hydrogen line, then by progressively injecting fluid into this line, while maintaining the air flow of conditions OP1 and OP2. It was observed that the separation is accentuated in the corner, at the entrance of the conical convergent, when the flow in the hydrogen line decreases.

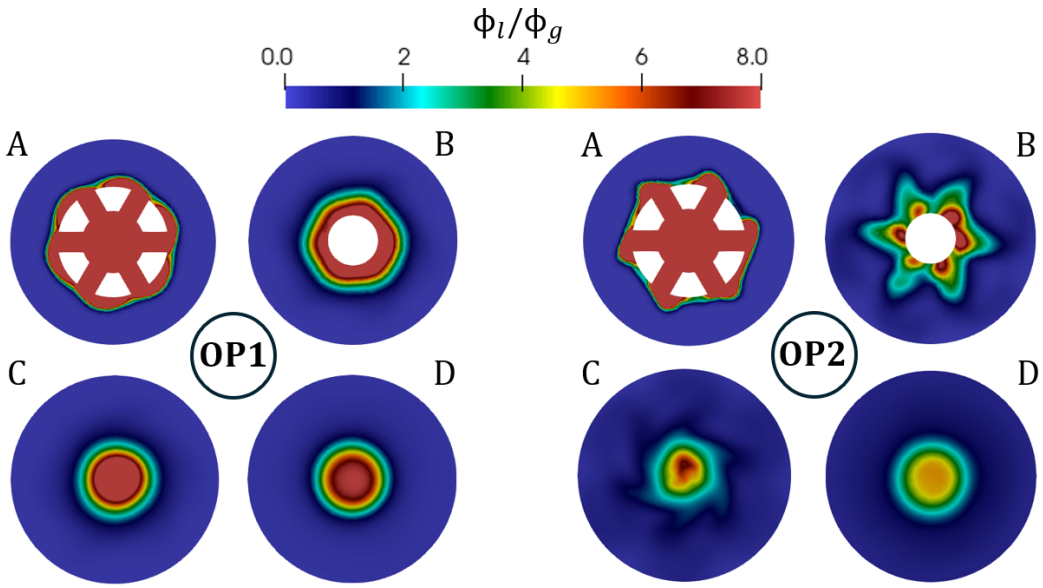

Figure 6: The ratio between local and global equivalence ratios ϕ_l/ϕ_g is shown for OP1 (left) and OP2 (right) in cold conditions, at 4 cross-sections A, B, C and D located inside the burner. These positions are indicated in Fig. 5 (left).

The paths that air and hydrogen follow are not as direct as in the OP1 case, resulting in slightly longer time duration spent in this area. In [14], for the same burner, hydrogen streamlines were calculated using Ivanov's analytical model for various cases with different hydrogen injection velocities, all demonstrating a similar flow structure, with weak hydrogen penetration. The reason for this behaviour is due to the very low hydrogen/air momentum flux ratio $J = \rho_{H_2} v_{H_2}^2 / \rho_a v_a^2$, which is caused by the very low hydrogen density.

For both cases the hydrogen follows the injector wall almost to the tip of the hydrogen injection cone, where it encounters the inner axial recirculating zone induced by the strong swirling air (see the blue axial zone in Fig. 4). At the burner outlet, the flow is accelerated because the presence of the internal

recirculating zone reduces the passage section. Due to the shear between the outgoing jet and this inner recirculating zone, the flow fluctuations are very high around $r = 2$ mm (see Fig. 3, right), which contributes greatly to mixing hydrogen and air.

In Fig. 5, the equivalence ratio fields are shown for both OP1 and OP2. It is evident that the mixing is almost complete at the end of the inner recirculating zone. For OP1, the mixing occurs primarily above the burner outlet, while for OP2, it occurs above the top of the hydrogen injector cone. In Fig. 5, right, the local equivalence ratio Φ_l is normalized with the global equivalence ratio Φ_g, which is 0.42 for OP1 and 0.20 for OP2. The mixing appears to be faster for the OP2 case. For this one, at the burner outlet, Φ_l/Φ_g is about 3, but it is close to 1 at 10 mm from the burner outlet. It should be noted that the mixing is partially achieved before the burner outlet in this case. For OP1, Φ_l/Φ_g is around 7 at the burner outlet, but it is less than 2, 10 mm from the exit. In the OP1 case, the mixing starts mainly at the bottom of the axial recirculating zone and it is then effective. Generally, the size of the recirculating zone is slightly longer than one outlet diameter, but it remains modest compared to the size of the combustion chamber. To complete these results, it is interesting to look at the distribution of the mixture inside the burner in transverse sections (Fig. 6). Four positions are chosen. They are indicated by dotted lines marked A, B, C and D in Fig. 5 (left). In case of OP1, section A, located at the axis of the radial hydrogen holes, there is no hydrogen penetration into the air. The hydrogen is distributed uniformly around the cone. In sections B and C, the hydrogen remains stuck around the cone, with a circular section. Mixing only takes

place much later, at the burner outlet hole. In case of OP2, the situation is very different. Hydrogen flows radially out of the holes for a short distance (section A), but it does not manage to lodge all around the cone. Air is present along the cone, between the hydrogen exit holes. In section B, located halfway up the cone, we see that the angles of the initial structure have stretched to form a six-pointed star. This elongation of the points promotes mixing. From section C, the central zone where the reduced equivalence ratio Φ_l/Φ_g is less than 6 (while Φ_g is 0.2), is very small. This low penetration of hydrogen has paradoxically contributed to the efficiency of the mixture. Injecting hydrogen in cross-flow, inside a swirl burner equipped with a conical nozzle, is therefore not prohibitive for achieving proper mixing at the outlet. Consequently, a significant portion of the reaction will occur in a zone with partially premixed components.

4.2. Flow characteristics under reactive conditions

The axial and azimuthal velocity profiles determined by LES, 2 mm downstream from the burner outlet, are compared to experiments in Fig. 7, for case OP1 under hot conditions. The LDA velocity measurements were taken with the air flow seeded by fine oil droplets. The consequence is that there is data only in areas with temperatures below 600 K. Similar to the cold flow results in section 2, the good agreement between the simulations and experiments indicates that the simulations can accurately predict the velocity field near the burner outlet in hot conditions. They are capable of capturing both the position of the stagnation points and the maximum values of the velocity fields. This validation is important for the rest of the study, because the

velocity field determines the position of the flame.

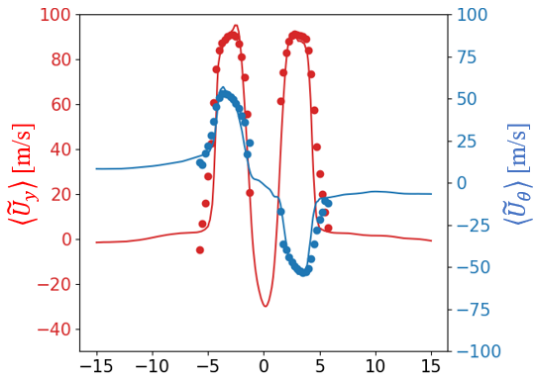

Figure 7: Radial profiles of mean axial and azimuthal velocities from LES (solid lines) and experiments (markers) at 1mm above the burner outlet for the case OP1 in hot conditions

.

Since the burner is not transparent, the entire flame may not be visible if part of it is inside. Measured and computed OH* mole fraction show that the simulations are able to capture the correct flame patterns, as well as the locations of the maximum normalized OH* values for both operating points. The distribution of HRR is quite different from the distribution of OH* inside the burner, especially for the OP1 flame (Fig. 8, upper row).

2D fields of averaged quantities (axial velocity, temperature and equivalence ratio) on the centerline plane are shown in Fig. 9. Although the HRR is present at the H2-injector tip for both operating conditions (Fig. 8), the temperature near the top of the injector is quite low for OP1 and OP2, below 1000 K. Experiments show that the injector tip did not have a red glow, which would typically indicate high temperatures. The flame foot is very thin near the tip of the cone. It follows that the heat transfer to the cone is relatively moderate and is consistent with experiments which show that the

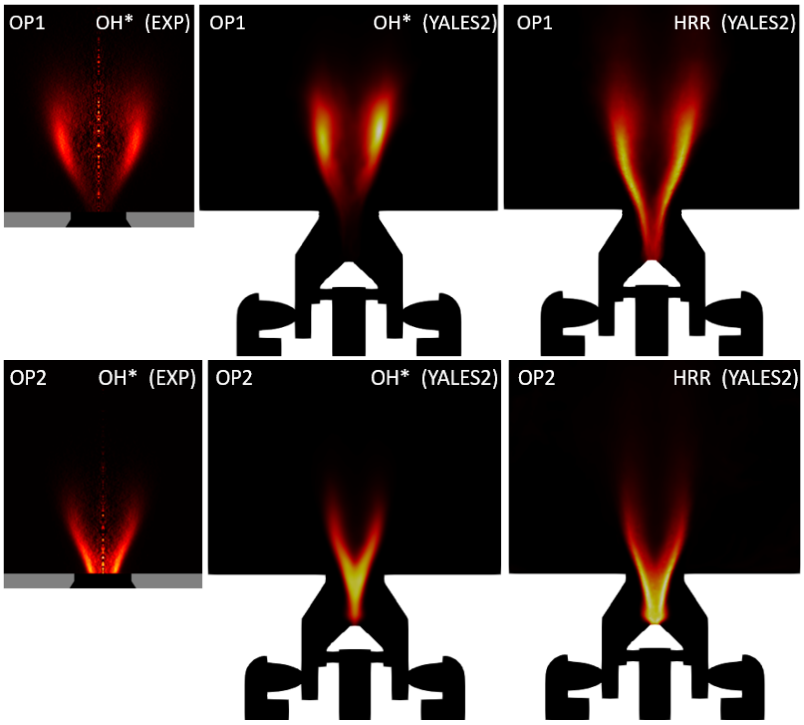

Figure 8: Comparisons between the OH* signal from experiments (left), the calculated time-averaged OH* mole fraction (middle) and HRR (right) obtained from the LES, for OP1 (upper row) and OP2.

injector tip did not have a red glow.

In Fig. 9, the time-averaged axial velocity fields are shown on the left for OP1 and OP2, respectively. For the case OP2, the bottom of the central recirculating zone reaches the top of the H2 injector, and the bottom of the zone is wider than in the OP1 case. The fact that the top of the cone is slightly truncated may contribute to this widening. In this zone, the combustion products recirculate, stabilizing the flame at the H2-injector tip. The flame stabilization effect at the injector tip can be observed in Fig. 8, as the normalized heat release rate value are high near the tip. For case OP2,

the maximum temperature (3rd column) is located slightly below the burner outlet and it reaches 1700 K. For both cases, OP1 and OP2, it is noted that there are no very hot areas near the walls inside the burner, even on the head of the hydrogen injector cone.

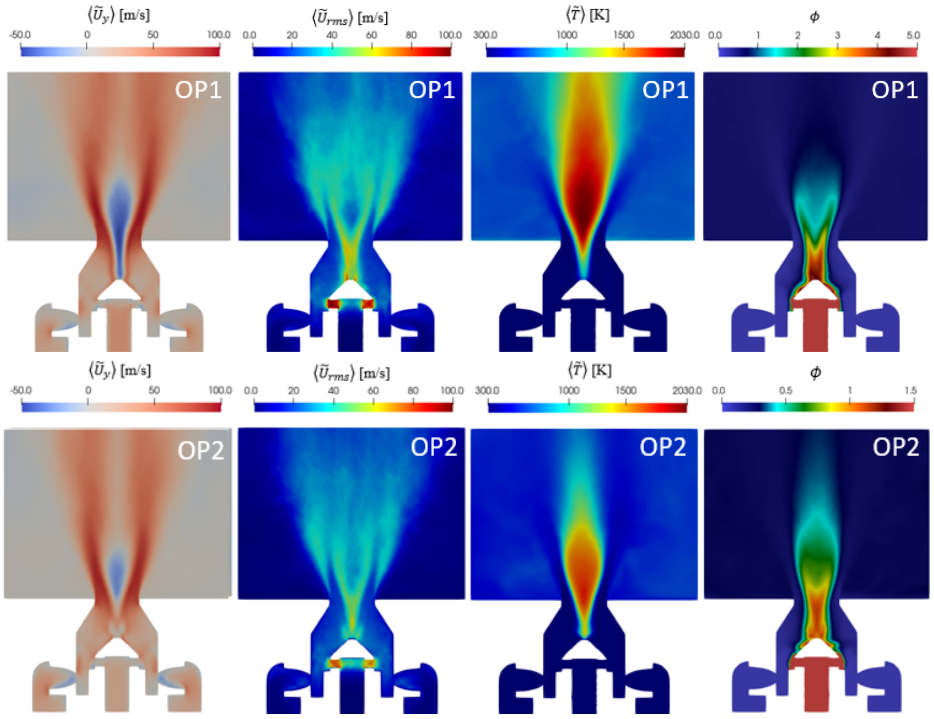

Figure 9: LES fields of axial averaged velocity (starting from the left), RMS axial velocity, temperature and relative equivalence ratio for OP1 (upper row) and OP2 (bottom row).

The RMS values of the axial velocity fluctuations are shown in the second column of Fig. 9. In both cases, OP1 and OP2, the values are notably high around and at the bottom of the axial recirculating zone. This indicates a significant shear of the flow, leading to strong mixing.

It is interesting to analyze the distribution of the mixture by plotting the equivalence ratio field (4th column). For the OP1 case, the distribution at

the burner outlet forms an "M" shape, with a hollow at the center. Regions with an equivalence ratio higher than 3 are confined inside the burner. At a distance from the burner outlet equal to 1.5 times the burner diameter, the equivalence ratio does not exceed 1. In case OP2, the mixing is well initiated from inside the burner, as in cold conditions (see Fig. 5, 2nd column). The central part does not exceed an equivalence ratio of 0.8, and the ratio drops quickly below 0.5 above the burner. In the OP1 case, this central zone of slightly higher equivalence ratio compared to the global equivalence ratio (0.2) remains located near the burner outlet. Its length does not exceed 1.5 times the outlet diameter. These results confirm what was previously observed in cold conditions. The mixing remains effective when the flame is present.

4.3. Modes of combustion determined with the Takeno Index

Instantaneous fields for OH*, HRR and the Takeno flame index are shown in Fig. 10. Used to analyse the combustion mode [41], the Takeno index is defined here as $FI = \frac{\nabla Y_F \cdot \nabla Y_O}{|\nabla Y_F| \cdot |\nabla Y_O|}$, where Y_F is the mass fraction of the fuel, which in this case is hydrogen, while Y_O is the mass fraction of oxygen. A value of -1 for the bounding value indicates that the combustion mode is non-premixed, while a value of 1 indicates that the flame is in premixed mode. In the upper row of Fig. 10 (case OP1), significant non-premixed combustion modes are observed at the top of the flame. In contrast, for condition OP2 (bottom row), there is a very small region with a blue color visible on the Takeno index map. This suggests that the mixture is overall more effective for OP2 than for OP1. However, inside the burner, between the conical top of

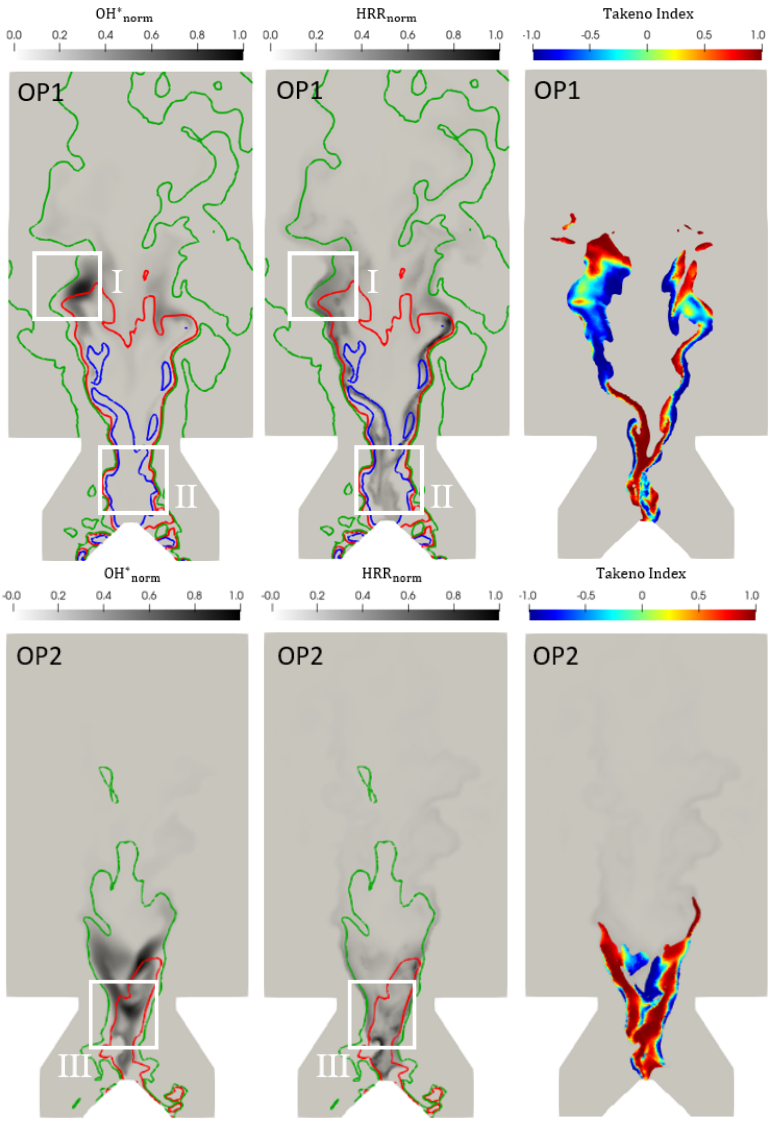

Figure 10: Comparisons between (from left to right) the instantaneous OH* mole fraction, HRR and Takeno Index from the LES, for OP1 (upper row) and OP2 (bottom row). The blue, red and green contour lines in OH* and HRR fields represent the equivalence ratios of 2.5, 1.0 and 0.5 respectively. For the Takeno Flame Index, the blue and red zones respectively represent non-premixed and premixed modes of combustion.

the hydrogen injector and the circular outlet, the combustion remains mainly of the premixed type in the OP1 case, even though the elongated red zone is somewhat narrow. In the case OP2, the Takeno index is close to 1 inside the burner's central zone, indicating that the combustion is of the premixed type. These results confirm that the mixing of hydrogen with air is efficient with cross-flow hydrogen injection, provided that there is a strongly swirled air flow. It is also likely that the converging conical nozzle contributes to the quality of the mixture by reducing the outlet section and increasing the flow shear.

In the snapshots of OH* and HRR shown in Fig. 10, the distribution of HRR is more prominent than the distribution of OH* for the case OP1. In zone I (top of Fig. 10, left and middle), both the presence of OH* and a significant distribution of HRR can be observed. However, in zone II, where the equivalence ratio is higher than 3, while the distribution of HRR is significant, there is no OH* emission. In case OP2, the areas showing the distribution of HRR and OH* are much more similar than in case OP1. It should be noted that downstream of the burner, the equivalence ratio in the flame zone is significantly less than 1 for OP2. On the other hand, in zone III, near the top of the injector cone, the distribution of HRR occupies a larger surface than that of OH*, where the equivalence ratio corresponds to a rich combustion (see Fig. 9 bottom right). However, in both cases studied, it is always observed that if there is an OH* emission, it is always in a zone close to an HRR distribution. Conversely, it is possible to have distributions of HRR without necessarily observing OH* emissions. On the OH* and HRR fields, three equivalence ratio lines are plotted: $\Phi = 0.5, 1$ and 2.5. In all the

areas examined, when the OH* emission is significant, a stoichiometric line is nearby. If the HRR distribution is intense in an area, but the equivalence ratio is far from stoichiometry in that zone, the OH* emission is low or almost nonexistent.

Even though it is clear that the OH* emission does not match the heat release rate distribution in partially premixed flames, it is still worth exploring the connection between these two factors. We have just established that the equivalence ratio is a significant factor, but based on the studies mentioned in the introduction [20, 25], it's also conceivable that the stretch plays a role in this relationship. The dependence between OH*, HRR, the equivalence ratio, and the strain rate is therefore examined in the next section.

5. 1-D counterflow premixed configuration analysis

To analyse the previous results, 1-D counterflow laminar premixed H2-air flame simulations are performed to determine OH* concentration and HRR distribution. The calculations were carried out at a pressure of 1 atm. The H2-air mixture is injected from the right, and pure air is injected from the left, both at a temperature of 300 K. The stagnation point is located at $x = 0$. For these calculations, the strain rate is set at 300 s^{-1}, which falls within the range of the strain rates calculated by LES for the flows in OP1 and OP2 operating conditions. It will be shown, at the end of this section, that the dependence on the strain rate remains moderate.

Figures 11 and 12 show the axial profiles of temperature, HRR, and OH* and OH mole fractions for a range of equivalence ratios between 0.47 and 1.0 for the first figure, and between 1.15 and 2.5 for the second. The premixed

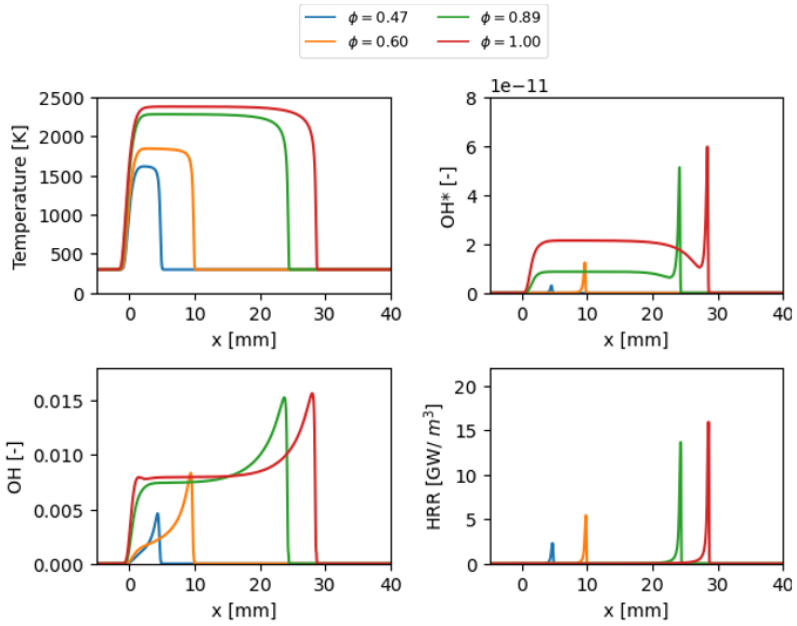

Figure 11: Axial profiles of temperature (top left), OH* mole fraction (top right), OH mole fraction (bottom left), and HRR (bottom right) for different lean and stoichiometric equivalence ratios of the fresh gases. The strain rate is 300 s^{-1}.

flame front is located on the right, far from the stagnation point, and it ranges from $x = 5$ mm for $\Phi = 0.47$ to $x = 37$ mm for $\Phi = 1.5$. Downstream the premixed flame front, up to the stagnation point, a plateau corresponding to the thermodynamic equilibrium is observed. Rich cases with Φ above 1.15 exhibit a double flame structure. In addition to the premixed flame front, a diffusion flame front appears around the stagnation point.

The heat release rate mainly occurs in the premixed flame front, while the profiles of OH and OH* mole fractions show peaks both at the premixed and at the diffusion front for rich flames. It was verified, by looking precisely at the position of the HRR and OH* peaks in the premixed flame front, that

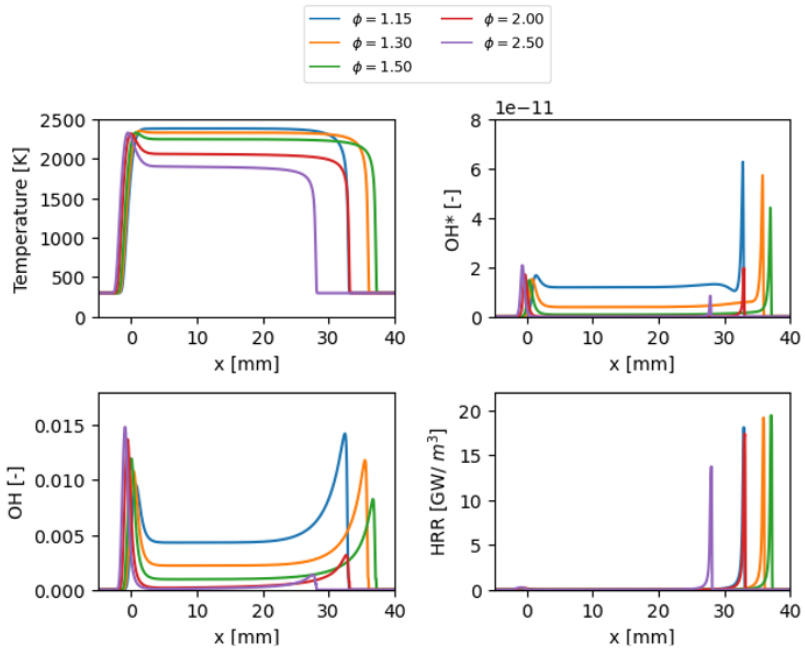

Figure 12: Axial profiles of temperature (top left), OH* mole fraction (top right), OH mole fraction (bottom left), and HRR (bottom right) for rich equivalence ratios of the fresh gases. The strain rate is 300 s^{-1}.

there is indeed a small gap between the two peaks, as indicated in [27]. As in this publication, the HRR peak of the present study is located upstream of the OH* peak by 1.8 tenths of a mm, which is analogous to the distance determined in [27], estimated to 2 tenths of a mm. For the sake of brevity, this gap is not shown here.

There is obviously a presence of OH in the burnt gases, with a plateau for equivalence ratios higher than 0.8. It is important to note that for equivalence ratios between 0.9 and 1.3, also the level of OH* remains high in the burnt gases, in the zone between the premixed flame front and the stagnation point, with a maximum level close to the stoichiometry. The values of the

temperature and the OH and OH* mole fractions obtained in the plateau of burnt gases are in accordance with those obtained using classical thermodynamic equilibrium computations by minimizing the Gibbs energy Based on the authors' knowledge, it appears that the presence of OH* in the burned gases of premixed hydrogen-air flames close to the stoichiometry has not been reported in the literature.

To ensure that this is not an artifact of the OH* mechanisms, this phenomenon has been verified experimentally with a premixed flame at different equivalence ratios. A Bunsen-like burner with a 6 mm wide outlet diameter was used to operate with premixed H_2/Air flames at fifteen equivalence ratios ranging from 0.6 to 2. The power varied from 0.71 kW to 1.79 kW. The air and hydrogen flows were mixed 2.5 m upstream of the burner outlet to ensure full premixing. During the experiment, the air flow rate was kept constant, while only the hydrogen flow rate was changed. The flames were somewhat turbulent, with a turbulence rate of 6 % at the burner exit. This turbulence was due to the high Reynolds number in the tube, which was higher than 5,100 for the chosen operating points. These high flow rates were selected to prevent flashback. The images were captured and averaged using an intensified camera equipped with an OH* filter centered at 310 nm. The light emissions were then processed using an Abel inversion to isolate only a slice of the light emission passing through the axis. Four representative images, shown in false colors, are presented in Fig. 13 after the post-processing. The vertical profiles of OH* intensity along a line parallel to the axis are depicted in Fig. 14 for the fifteen different operating conditions. This line is 0.5 mm away from the axis to avoid the mathematical indeterminacy on the

symmetry axis caused by the Abel transform. It is drawn as a dotted line in the first image (Fig. 13). The z axial coordinate is divided by the measured flame length L_f to correct for the effect of the equivalence ratio on the flame front location. The presence of OH^* radical in the burnt gases shows a plateau over $z/L_f = 1.5$ for equivalence ratios between 0.8 and 1.3, which is consistent with the numerical results presented in Fig. 11. In the experiment, a spectrometer was used to confirm that the light signal captured by the camera in the burned gases matched the chemiluminescent emission of the OH* radical. It was observed that the level of OH* in the burned gases, in comparison to the level of OH* in the flame front, was lower than what was obtained in the 1-D calculations (Figs. 11 and 12). This level is not negligible. The variation in relative levels between the experiment and the 1-D calculation may be attributed to the flame not being perfectly adiabatic, leading to lower burnt gas temperatures in the experiment compared to the simulation.

The presence of OH* in the burned gases of hydrogen flames near stoichiometry can change the interpretation when observing the OH* signal of a flame as a whole, for example, using a photomultiplier to measure the OH* emission of the entire flame. Typically, one can be interested in using the OH* emission only from the flame front. It would therefore be necessary to spatially filter this emission coming from the burnt gases, which can be very complicated in the case of swirled flames presenting a strong recirculating of hot gases on the axis of the burner.

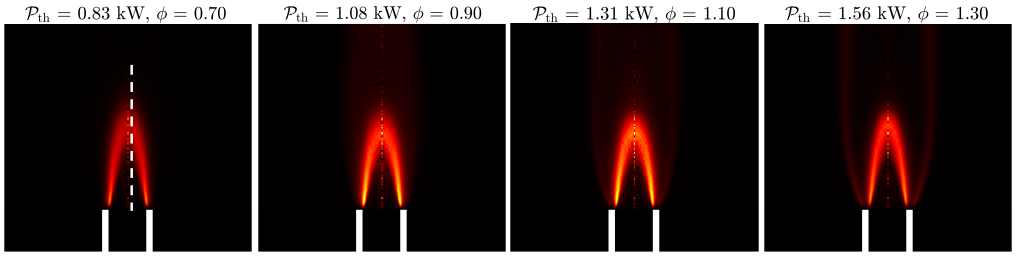

Figure 13: OH* emission from premixed H2/air flames, following an Abel inversion. The equivalence ratios for the four images from left to right are 0.70, 0.90, 1.1, and 1.30 respectively. In the first image, a dotted vertical line is included to indicate the location where OH* profiles are extracted.

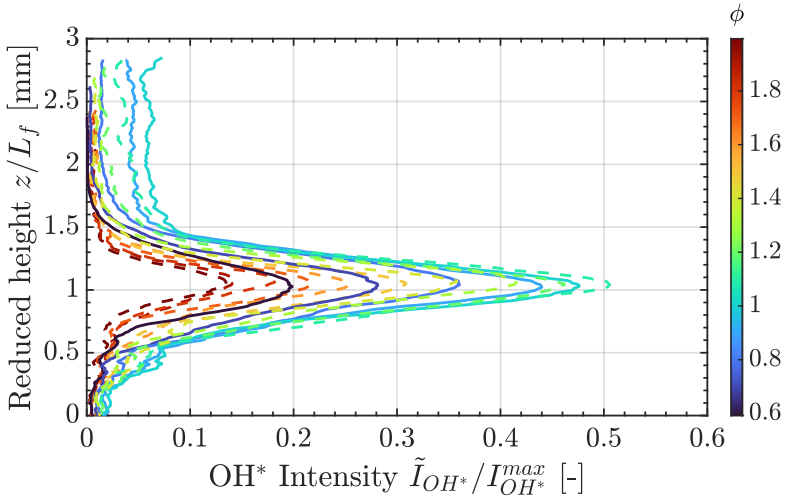

Figure 14: Vertical profiles of OH* intensity calculated from Abel-inverted chemiluminescence images. The starting point of the graph, $z/L_f = 0$, is at the burner outlet.

To verify if the significant presence of OH* in the burnt gases is related to the very high temperature of combustion products, additional 1-D computations of freely-propagating premixed flames have been performed with preheated fresh gases. OH* profiles are presented in Fig. 15 (left) for fresh gases at 300K, 500K and 700K, for the equivalence ratio of 1.0. The fresh

mixture is injected from the left. By increasing the temperature of the fresh gases, the levels of the OH* in the burnt gases rise significantly, as compared to the OH* peak. The OH* mole fractions in the burnt gases obtained from the 1-D computations are then compared to the values obtained from the thermodynamic equilibrium computations in Fig. 15 (right). In this figure we can see the strong increase of OH* in the combustion products with the preheating temperature. The results are presented versus the equivalence ratio. This suggests that the presence of significant OH* levels in the burnt gases, observed in Figs. 11 and 12, is due to the higher flame temperatures close to stoichiometry, and therefore to more excited state of OH, since this radical is present in the combustion products. Since with highly preheated H_2/air flames, the OH* concentration in the burnt gases can be even higher than in the flame front, one should be careful when using OH* as a marker for heat release rate under these conditions.

In Figures 11 and 12, it is noticed that at the location of the premixed flame front, the intensity of the peaks of HRR and OH* varies with the equivalence ratio, but not in the same way. The OH* peak is diminished more strongly at rich conditions. $\Omega_{HRR} = peak(HRR)_\Phi / Max\Big(peak(HRR)_\Phi\Big)$ and $\Omega_{OH*} = peak(Y_{OH*})_\Phi / Max\Big(peak(Y_{OH*})_\Phi\Big)$, where 'peak' refers to the maximum value for a particular equivalence ratio and 'Max' to the maximum value among all of the equivalence ratios, are plotted in Fig. 16 for $0.3 < \phi < 4.0$. The calculations were conducted for different strain rates ranging from 150 s^{-1} to 6000 s^{-1}, knowing that the maximum strain rate values observed in the LES simulation are of the order of 1000 s^{-1}. The maximum of the OH* fraction is located around $\Phi = 1.2$, while the maximum for HRR is around

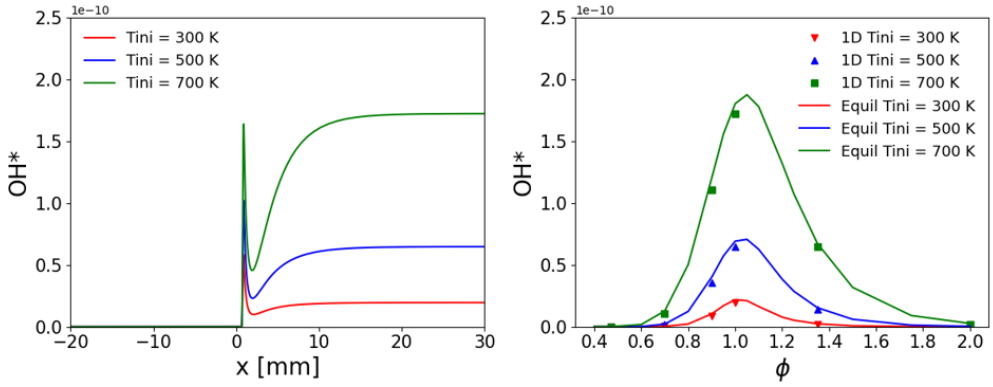

Figure 15: Left: OH* mole fraction profiles in the 1-D domain, for temperatures of the fresh gases (Tini) at 300K, 500K and 700K, for equivalence ratio of 1. Right: Comparisons of the OH* values in the burnt gases obtained from 1-D computations (symbols) and from the equilibrium calculations (lines) for temperatures of fresh gases at 300K, 500K and 700K, with respect to the equivalence ratio.

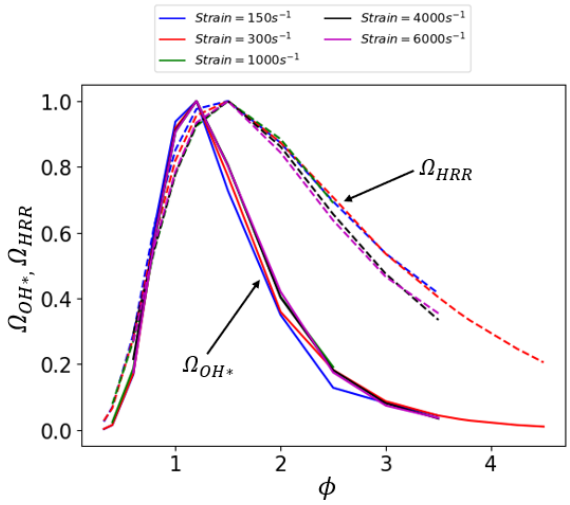

Figure 16: Variations of Ω_{HRR} and Ω_{OH*} as a function of the equivalence ratio for different strain rates.

1.6-1.7. It is observed that the dependence on strain of premixed hydrogen-air flames remains low. All the curves remain close whatever the strain rate.

In rich regions, however, a strong departure between Ω_{HRR} and Ω_{OH*} is observed. In the case of partially premixed flames, variations of the mixing ratio in a flame mean that the OH* peak in the case of partially premixed flames is not directly proportional to the heat release rate in fuel rich regions. In terms of experimental diagnostics, OH* acts as an approximate marker of the heat release rate in lean partially-premixed flames with an overall equivalence ratio less than 0.8, while knowing the reservations expressed in [27] on the coincidence of OH* and HRR peaks.

In light of the results on the evolution of the Ω coefficients, it is interesting to re-examine the images in Fig. 10. For OP1 (upper row), the value of Φ ranges from 0.8 to 1.5 in zone I. As a result, Ω_{HRR} and Ω_{OH*} are close to 1, allowing for the detection of high HRR by OH*. Moving on to zone II, the equivalence ratio reaches up to 2.5, leading to a more significant reduction in the OH* field compared to the HRR. In the case of OP2, there is a high concentration of OH* and HRR below the injector outlet, in an area where the equivalence ratio is near stoichiometry.

6. Conclusions

In this study, Large Eddy Simulations (LES) of a swirled partially-premixed hydrogen-air flame with cross-flow hydrogen injection are performed under two operating conditions: at equivalence ratios of 0.2 and 0.42, to have two types of flames. This research represents the first numerical investigation of a partially-premixed pure hydrogen flame with cross-flow injection. The results from the simulations using LES are compared to the experimental results in terms of the axial and tangential velocity distributions near the

burner outlet, for both non-reacting (cold flow) and reacting flow conditions. The comparison shows good agreement.

In cold flow conditions, the velocity field inside the burner is studied by LES to understand how mixing happens. Because the momentum flux ratio is low, the injected hydrogen can't go directly into the air flow. However, once the hydrogen reaches the top of the hydrogen injector, where the swirling air flow creates an internal recirculating zone, the mixing becomes very efficient. This effect occurs slightly upstream of the burner outlet, and it is increased by the presence of a converging nozzle. It should be noted that the mixing is most efficient with the lowest hydrogen flow rate. The mixing process ends at the burner outlet, over a distance of less than two diameters. With this type of burner, cross-flow hydrogen injection does not seem to be a disadvantage, as the swirled flow plays a crucial role in driving the mixing process.

In cases of reacting flow, LES accurately predicts the position of the OH* emission. Although the flame at the richer operating condition appeared lifted on the OH* images, the computations show that it is attached to the injector tip as significant heat release rate can be observed in this region. The simulations also show that the OH* values are highest in regions close to the stoichiometric conditions. The heat release rate (HRR) and OH* fields obtained from LES are then compared. Significant differences are observed between the two fields. The OH* images do not correspond well to the HRR images, especially near the base of the flames, in areas where the equivalence ratio is much higher than 1.

To understand this behavior, computations, using 1-D counterflow premixed flame, were performed for a series of equivalence ratios, from 0.4 to 2.5.

The results show that the highest OH* peak value is around an equivalence ratio of 1.2, while the highest peak of HRR is at $\phi = 1.6 - 1.7$. The amplitude of the peaks decreases very quickly moving away from stoichiometry, but on the side of the rich flames, the OH* peak falls much more quickly than that of the HRR. On the lean flame side, the decay of the OH* peak presents a similarity with that of the HRR peak, which tends to show a possible link between HRR and OH* in these lean flame conditions.

1-D simulations also showed a particular aspect of hydrogen-air flames. When they are close to stoichiometry, an OH* emission appears in the burnt gases, due to the high temperatures encountered and to thermodynamic equilibrium. This phenomenon has been verified experimentally. Even if this emission remains moderate for stoichiometric flames with fresh gases at ambient temperature, it cannot be neglected, especially if there is a preheating of air, which is the case in the combustion chambers of aeronautical engines, or in gas turbines. This effect prevents the use of the OH* signal, emitted by the entire flame, as a marker of the heat release rate for premixed flames close to stoichiometry, especially if the reactants are preheated.

Acknowledgments

This research was funded by the Fondation Simone and Cino Del Duca through a scientific grant attributed to the project PLATHON and by the FlyHy project of the Agence Nationale de la Recherche (ANR-21-CE05-0008). A CC-BY public copyright license has been applied by the authors to the present document and will be applied to all subsequent versions up to the Author Accepted Manuscript arising from this submission. This research was conducted using HPC resources from IDRIS, TGCC, and CINES under the

allocation A0132B10253 by GENCI (Grand Equipement National de-Calcul Intensif). The code YALES2 was used. Vincent Moureau and Ghislain Lartigue are acknowledged for their technical support. Prof. Sébastien Candel and Dr. Nicolas Minesi are thanked for fruitful discussions.

References

[1] T. Sattelmayer, C. Mayer, J. Sangl, Interaction of flame flashback mechanisms in premixed hydrogen–air swirl flames, J. Eng. Gas Turbines Power 138 (2016) 011503.

[2] M. Day, J. Bell, R. Cheng, S. Tachibana, V. Beckner, M. Lijewski, Cellular burning in lean premixed turbulent hydrogen-air flames: coupling experimental and computational analysis at the laboratory scale, J. Phys. Conf. Ser. 180 (2009) 012031.

[3] X. Yang, W. Yang, S. Dong, H. Tan, Flame stability analysis of premixed hydrogen/air mixtures in a swirl micro-combustor, Energy 209 (2020) 118495.

[4] F. H. Vance, L. De Goey, J. A. van Oijen, Development of a flashback correlation for burner-stabilized hydrogen-air premixed flames, Combust. Flame 243 (2022) 112045.

[5] A. Aniello, T. Poinsot, L. Selle, T. Schuller, Hydrogen substitution of natural-gas in premixed burners and implications for blow-off and flashback limits, Int. J. Hydrog. Energy 47 (2022) 33067–33081.

[6] A. Aniello, D. Laera, S. Marragou, H. Magnes, L. Selle, T. Schuller, T. Poinsot, Experimental and numerical investigation of two flame stabilization regimes observed in a dual swirl H2-air coaxial injector, Combust. Flame 249 (2023) 112595.

[7] M. Leroy, C. Mirat, A. Renaud, R. Vicquelin, Stabilization of low-NOx hydrogen flames on a dual-swirl coaxial injector, J. Eng. Gas Turbines Power 145 (2023) 021021.

[8] S. Marragou, T. F. Guiberti, T. Poinsot, T. Schuller, Near-field mixing in a coaxial dual swirled injector, Flow, Turbulence and Combustion (2024) 1–22.

[9] H.-W. Funke, S. Börner, J. Keinz, K. Kusterer, D. Kroniger, J. Kitajima, M. Kazari, A. Horikawa, Numerical and experimental characterization of low nox micromix combustion principle for industrial hydrogen gas turbine applications, in: Turbo Expo: Power for Land, Sea, and Air, Vol. 44687, American Society of Mechanical Engineers, 2012, pp. 1069–1079.

[10] H.-W. Funke, J. Keinz, K. Kusterer, A. H. Ayed, M. Kazari, J. Kitajima, A. Horikawa, K. Okada, Development and testing of a low NOx micromix combustion chamber for industrial gas turbines, Int. J. Gas Turbine Propuls. Power Syst. 9 (2017) 27–36.

[11] H.-W. Funke, N. Beckmann, S. Abanteriba, An overview on dry low NOx micromix combustor development for hydrogen-rich gas turbine applications, Int. J. Hydrog. Energy 44 (2019) 6978–6990.

[12] J.-B. Perrin-Terrin, N. Vaysse, D. Durox, R. Vicquelin, S. Candel, C. Laux, A. Renaud, Plasma-assisted combustion of hydrogen swirling flames: extension of lean blow-off limit and NOx emissions, accepted at Symposium (international) on combustion (2024).

[13] N. Vaysse, D. Durox, R. Vicquelin, S. Candel, A. Renaud, Stabilization and dynamics of pure hydrogen swirling flames using cross-flow injection, Turbo Expo: Power for Land, Sea, and Air 86953 (2023) V03AT04A043.

[14] N. Vaysse, D. Durox, P. R. Soundararajan, R. Vicquelin, S. Candel, A. Renaud, Structure and light emission of swirling flames produced by pure hydrogen injection in cross-flow, 11th European Combustion Meeting (2023).

[15] S. Karyeyen, J. S. Feser, A. K. Gupta, Hydrogen concentration effects on swirl-stabilized oxy-colorless distributed combustion, Fuel 253 (2019) 772–780.

[16] S. Böckle, J. Kazenwadel, T. Kunzelmann, D.-I. Shin, C. Schulz, J. Wolfrum, Simultaneous single-shot laser-based imaging of formaldehyde, OH, and temperature in turbulent flames, Proc. Combust. Inst. 28 (2000) 279–286.

[17] R. L. Gordon, A. R. Masri, E. Mastorakos, Heat release rate as represented by [OH] × [CH2O] and its role in autoignition, Combust. Theory Model. 13 (2009) 645–670.

[18] I. Hurle, R. Price, T. M. Sugden, A. Thomas, Sound emission from open turbulent premixed flames, Proc. R. Soc. London A 303 (1968) 409–427.

[19] B. Higgins, M. McQuay, F. Lacas, J.-C. Rolon, N. Darabiha, S. Candel, Systematic measurements of OH chemiluminescence for fuel-lean, high-pressure, premixed, laminar flames, Fuel 80 (2001) 67–74.

[20] M. Lauer, M. Zellhuber, T. Sattelmayer, C. J. Aul, Determination of the heat release distribution in turbulent flames by a model based correction of OH* chemiluminescence, J. Eng. Gas Turb. Pow. 133 (2011) 121501.

[21] L. He, Q. Guo, Y. Gong, F. Wang, G. Yu, Investigation of OH* chemiluminescence and heat release in laminar methane–oxygen co-flow diffusion flames, Combust. Flame 201 (2019) 12–22.

[22] S. Yan, Y. Gong, Z. Duan, Q. Guo, G. Yu, Investigation of the correlation between OH*, CH* chemiluminescence and heat release rate in methane inverse diffusion flame, Energy 283 (2023) 129162.

[23] J. Ballester, R. Hernández, A. Sanz, A. Smolarz, J. Barroso, A. Pina, Chemiluminescence monitoring in premixed flames of natural gas and its blends with hydrogens, Proc. Combust. Inst. 32 (2009) 2983–2991.

[24] B. Prabasena, M. Röder, T. Kathrotia, U. Riedel, T. Dreier, C. Schulz, Strain rate and fuel composition dependence of chemiluminescent species profiles in non-premixed counterflow flames: comparison with model results, Appl. Phys. B 107 (2012) 561–569.

[25] S. Meng, S. Wu, M. Zhang, Numerical and experimental study of flow structure and heat release distribution in a stratified swirl flame with high-speed PIV and OH, AIP Adv. 11 (2021).

[26] M. Ferrarotti, R. Amaduzzi, D. Bascherini, C. Galletti, A. Parente, Heat release rate markers for the adelaide jet in hot coflow flame, Front. Mech. Eng. 6 (2020).

[27] F. Schiavone, A. Aniello, E. Riber, T. Schuller, D. Laera, On the adequacy of oh* as heat release marker for hydrogen-air flames, Proceedings of the Combustion Institute 40 (1) (2024) 105248. doi:https://doi.org/10.1016/j.proci.2024.105248.

[28] G. Vignat, P. R. Soundararajan, D. Durox, A. Vié, A. Renaud, S. Candel, A joint experimental and large eddy simulation characterization of the liquid fuel spray in a swirl injector, J. Eng. Gas Turb. Pow. 143 (2021).

[29] M. Vanpee, R. Mainiero, The spectral distribution of the blue hydrogen flame continuum and its origin in hydrogen nitric oxide flames, Combust. Flame 34 (1979) 219–230.

[30] T. Fiala, T. Sattelmayer, S. Gröning, J. Hardi, R. Stützer, S. Webster, M. Oschwald, Comparison between excited hydroxyl radical and blue radiation from hydrogen rocket combustion, J. Propul. Power 33 (2017) 490–500.

[31] V. Moureau, P. Domingo, L. Vervisch, Design of a massively parallel CFD code for complex geometries, C. R. Mécanique 339 (2011) 141–148.

[32] M. Germano, U. Piomelli, P. Moin, W. H. Cabot, A dynamic subgrid-scale eddy viscosity model, Phys. Fluids A 3 (1989) 1760–1765.

[33] https://web.eng.ucsd.edu/mae/groups/combustion/ mechanism.html.

[34] D. Alviso, J. Rolon, P. Scouflaire, N. Darabiha, Experimental and numerical studies of biodiesel combustion mechanisms using a laminar counterflow spray premixed flame, Fuel 153 (2015) 154–165.

[35] G. Ferrante, G. Eitelberg, I. Langella, Differential diffusion modelling for les of premixed and partially premixed flames with presumed FDF, Combust. Theory Model. (2024) 1–36.

[36] J. Leparoux, R. Mercier, S. Puggelli, M. Cailler, V. Moureau, Numerical investigation of a hydrogen–air flame for NOx prediction, J. Eng. Gas Turb. Pow. 146 (2024).

[37] T. Kathrotia, M. Fikri, M. Bozkurt, M. Hartmann, U. Riedel, C. Schulz, Study of the H+ O+ M reaction forming OH*: Kinetics of OH* chemiluminescence in hydrogen combustion systems, Combust. Flame 157 (2010) 1261–1273.

[38] G. Smith, J. Luque, C. Park, J. Jeffries, D. Crosley, Low pressure flame determinations of rate constants for OH (a) and CH (a) chemiluminescence, Combust. Flame 131 (1-2) (2002) 59–69.

[39] F. Charlette, C. Meneveau, D. Veynante, A power-law flame wrinkling model for LES of premixed turbulent combustion part i: non-dynamic formulation and initial tests, Combust. Flame 131 (2002) 159–180.

[40] J. P. Legier, T. Poinsot, D. Veynante, Dynamically thickened flame LES model for premixed and non-premixed turbulent combustion, Proc. Summer Program. Cent. Turbul. Res. (2000) 157–168.

[41] T. T. H. Yamashita, M. Shimada, A numerical study on flame stability at the transition point of jet diffusion flames, Symp. (Int.) Combust. 26 (1996) 27–34.